



Numerical Investigation on the Effect of the Oxymethylene Ether-3 (OME₃) Blending Ratio in Premixed Sooting Ethylene Flames

Robert Schmitz^{1*}, Mariano Sirignano², Christian Hasse¹ and Federica Ferraro¹

¹Institute for Simulation of Reactive Thermo-Fluid Systems (STFS), Technical University of Darmstadt, Darmstadt, Germany,

²Dipartimento di Ingegneria Chimica, dei Materiali e della Produzione Industriale, Università degli Studi di Napoli Federico II, Napoli, Italy

OPEN ACCESS

Edited by:

Raul Payri,
Universitat Politècnica de València,
Spain

Reviewed by:

Vasudevan Raghavan,
Indian Institute of Technology Madras,
India

Dong Han,
Shanghai Jiao Tong University, China

Chun Lou,
Huazhong University of Science and
Technology, China

*Correspondence:

Robert Schmitz
schmitz@stfs.tu-darmstadt.de

Specialty section:

This article was submitted to
Engine and Automotive Engineering,
a section of the journal
Frontiers in Mechanical Engineering

Received: 19 July 2021

Accepted: 16 August 2021

Published: 27 August 2021

Citation:

Schmitz R, Sirignano M, Hasse C and
Ferraro F (2021) Numerical
Investigation on the Effect of the
Oxymethylene Ether-3 (OME₃)
Blending Ratio in Premixed Sooting
Ethylene Flames.
Front. Mech. Eng 7:744172.
doi: 10.3389/fmech.2021.744172

Synthetic fuels, especially oxygenated fuels, which can be used as blending components, make it possible to modify the emission properties of conventional fossil fuels. Among oxygenated fuels, one promising candidate is oxymethylene ether-3 (OME₃). In this work, the sooting propensity of ethylene (C₂H₄) blended with OME₃ is numerically investigated on a series of laminar burner-stabilized premixed flames with increasing amounts of OME₃, from pure ethylene to pure OME₃. The numerical analysis is performed using the Conditional Quadrature Method of Moments combined with a detailed physico-chemical soot model. Two different equivalence ratios corresponding to a lightly and a highly sooting flame condition have been investigated. The study examines how different blending ratios of the two fuels affect soot particle formation and a correlation between OME₃ blending ratio and corresponding soot reduction is established. The soot precursor species in the gas-phase are analyzed along with the soot volume fraction of small nanoparticles and large aggregates. Furthermore, the influence of the OME₃ blending on the particle size distribution is studied applying the entropy maximization concept. The effect of increasing amounts of OME₃ is found to be different for soot nanoparticles and larger aggregates. While OME₃ blending significantly reduces the amount of larger aggregates, only large amounts of OME₃, close to pure OME₃, lead to a considerable suppression of nanoparticles formed throughout the flame. A linear correlation is identified between the OME₃ content in the fuel and the reduction in the soot volume fraction of larger aggregates, while smaller blending ratios may lead to an increased number of nanoparticles for some positions in the flame for the richer flame condition.

Keywords: oxymethylene ether-3 (OME₃), PODE₃, soot particle formation, soot modeling, alternative fuels, Quadrature Method of Moments (QMOM)

1 INTRODUCTION

The ongoing tightening of emissions legislation is resulting in increasingly vigorous efforts to control the pollutants formed in hydrocarbon combustion systems in the transportation and power generation sectors. Synthetic fuels produced with renewable energy and, in particular, oxygenated fuels can improve both the overall carbon balance and local emissions, such as soot particles, without extensively modifying the present combustion devices. Oxymethylene ethers

(OMEs), which are promising synthetic fuel candidates (Kohse-Höinghaus, 2021), deployable e.g. in self-ignition engines, have been proven in recent studies (Ferraro et al., 2021; Tan et al., 2021) to significantly reduce the sooting tendency of blended fuel flames. Compared to other alternative and oxygenated fuel candidates such as biodiesels and alcohols, oxymethylene ethers combine high oxygenation of around 50% by mass (Wang et al., 2016) with high propensity for self-ignition (Lumpkin et al., 2011; Wang et al., 2016). While the combustion of pure OMEs exhibits almost the complete suppression of soot, an application as a blending fuel is a more realistically viable scenario in the short and medium term. The good miscibility of oxymethylene ethers in fossil diesel (Lin et al., 2019; Omari et al., 2019) supports this scenario. OME₃ to OME₅ in particular exhibit properties favourable to their use as fuel blends in compression ignition applications. For instance, the cetane number of OME₃ to OME₅ is in the range of 72–93 (Lautenschütz et al., 2016; 2017; Deutsch et al., 2017) and the flash, boiling and melting points are comparable to those of diesel fuel (Zheng et al., 2013; Omari et al., 2019). These suitable characteristics explain the recent research interest in this specific group of oxygenated fuels in the field of kinetic mechanism development (Sun et al., 2017; He et al., 2018; Cai et al., 2019; Li et al., 2020; Bai et al., 2021; Niu et al., 2021), their application in engine simulations (Lin et al., 2019; Lv et al., 2019; Ren et al., 2019) or for different synthesis methods (Gierlich et al., 2020; Klokic et al., 2020), and the assessment of the overall carbon impact (Mahbub et al., 2019; Bokinge et al., 2020). The application of oxymethylene ethers in engines in combination with their emission propensity has been investigated in several studies (Pellegrini et al., 2013; Barro et al., 2018; Huang et al., 2018; Liu et al., 2019; Ren et al., 2019; LeBlanc et al., 2020; Parravicini et al., 2020; Pélerin et al., 2020), while fewer investigations have been conducted, notably, into soot formation for pure or blended OMEs in canonical flames (Ferraro et al., 2021; Tan et al., 2021). Hence, this work addresses the potential of oxymethylene ether-3 (OME₃) and its effect on soot particle formation and growth to deeply understand the soot suppression phenomenon in a simple configuration and in blending with a well-known fuel such as ethylene. While studies containing small amounts of OME₃ blended into C₂H₄ have been performed for both premixed flames (Ferraro et al., 2021) and diffusion flames (Tan et al., 2021), the effects of blending increased amounts of OME₃ has not been investigated yet. Additionally, a systematic assessment between the blending ratio of OME_n fuels and their effects on the overall soot reduction and especially on the individual maturation steps in the soot evolution process is unknown to the authors. Detailed knowledge of the soot reduction potential including possible saturation effects for higher blending ratios is needed for an efficient application of synthetic fuels. Therefore, this study aims to analyze these aspects for OME₃ combustion. The correlation between the OME₃ blending ratio and the soot reduction will be numerically investigated. The analysis systematically evaluates the complete range of OME₃ blending ratios using detailed chemistry combined with a quadrivariate soot model enabling a deeper understanding

of the effects of different amounts of OME₃ blending on the entire soot formation process.

Simulations are performed on a series of laminar burner-stabilized premixed flames burning ethylene blended with increasing amounts of OME₃ up to a pure OME₃/air flame at constant equivalence ratios. Detailed chemical kinetics in combination with the Conditional Quadrature Method of Moments (CQMOM) (Salenbauch et al., 2017, 2018), based on the physico-chemical soot model by D'Anna et al. (2010), are chosen to model soot formation, particle surface growth and other occurring particle processes. This approach enables a detailed investigation of the soot suppression behavior of OME₃ regarding the smaller carbon chemistry, and of different particle size classes, such as large polycyclic aromatic hydrocarbons, spherical clusters and larger aggregates including their chemical properties. The effect that increasing amounts of OME₃ exert on soot formation is evaluated in terms of both the total soot volume fraction and the particle size distribution. Additionally, the relationship between the OME₃ to ethylene blending ratio and the subsequent soot reduction is analyzed to verify whether OME₃ has only a dilution effect on the mixture or if it also has an active kinetic effect in the formation of soot gas-phase precursors, nano-organic carbon and soot particles. Finally, the range of OME₃ blending ratios yielding a soot suppression effect is identified to assess the overall potential of this oxygenated fuel. This study is performed for two different equivalence ratios covering lightly to highly sooting flame conditions.

2 NUMERICAL MODELING

The numerical modeling includes a description of the gas-phase chemistry and of the soot particle formation and evolution. The gas-phase chemistry is modeled by a detailed kinetic mechanism accounting for 141 species and 674 reactions in total. The decomposition and oxidation reactions of OME₃ (41 species and 213 reactions) are taken from Sun et al. (2017). The reactions of smaller and larger carbon species up to polycyclic aromatic hydrocarbons (PAHs) are described by the kinetic mechanism by D'Anna et al. (2010), Sirignano et al. (2010, 2013), and Conturso et al. (2017).

To describe the soot particle evolution, the physico-chemical soot formation model (D'Anna et al., 2010) is combined with the Conditional Quadrature Method of Moments. The numerical approach was developed in Salenbauch et al. (2017) and has been successfully applied in atmospheric premixed flames (Salenbauch et al., 2017, 2018; Ferraro et al., 2021). A short summary is described in the following. The gas-phase kinetics consider species up to pyrene, while larger PAHs are treated as lumped species. The soot model distinguishes between three different particle structures based on their state of aggregation (D'Anna et al., 2010). Soot precursors with a molecular mass larger than pyrene (*molecules or large PAHs*) are classified separately from the spherically shaped, solid soot particles which are formed through the inception step of several PAHs (*clusters*), and *aggregates*. These in turn are formed due to the agglomeration of several clusters with subsequent soot maturation steps leading

to strongly bonded fractal-shaped particles. The physico-chemical nature of the soot model allows an assessment to be carried out based not only on the size and shape of the particles but also on their chemical properties such as the carbon to hydrogen ratio and their chemical reactivity. The soot processes are formulated based on Arrhenius-rate laws and include growth processes such as the H-Abstraction-C₂H₂-Addition (HACA) mechanism, the resonantly stabilized free radical mechanism or surface growth due to chemical processes. Surface growth and oxidation reactions are applied for all the three entities that describe the soot evolution such as large PAH, clusters and aggregates. Additionally, nucleation steps for different-sized large PAHs are accounted for, resulting in clusters with varying chemical properties as well as soot oxidation and oxidation-induced fragmentation, dehydrogenation and aggregation processes of several clusters, resulting in aggregates shaped like snowflakes, fractals or chains.

Due to the variety of the soot particles involved, classification and bundling similar to lumped species is necessary. The evolution of the chemical and physical properties of each particle class is described by the population balance equation (PBE) for the number density function (NDF) $f(\underline{\xi}; \underline{x}, t)$, which depends on the spatial coordinates \underline{x} , the time information t and the internal property vector $\underline{\xi} = [\xi_{nc}, \xi_{H/C}, \xi_{stat}, \xi_{typ}]^T$. This vector contains two continuous properties ξ_{nc} , indicating the number of carbon atoms with $\xi_{nc} \in [0, \infty)$, and $\xi_{H/C}$ describing the carbon to hydrogen ratio with $\xi_{H/C} \in [0, 1]$. ξ_{typ} and ξ_{stat} are discrete dimensions representing the type of entities $\xi_{typ} \in A$, $A = \{\text{large PAHs, clusters, aggregates}\}$, and ξ_{stat} the chemical reactivity with $\xi_{stat} \in B$, $B = \{\text{stable, radical}\}$. Applying Bayes's decomposition, the quadrivariate number density function $f(\underline{\xi}; \underline{x}, t)$ reads as follows

$$f(\underline{\xi}) = f_{H/C}(\xi_{H/C}|\xi_{nc}, \xi_{stat}, \xi_{typ}) \cdot f_{nc}(\xi_{nc}|\xi_{stat}, \xi_{typ}) \cdot n(\xi_{stat}, \xi_{typ}), \quad (1)$$

where the time and spatial dependencies are omitted for brevity.

Here, the distributions $f_{H/C}$ and f_{nc} are conditioned on the state $(\xi_{nc}, \xi_{stat}, \xi_{typ})$ and (ξ_{stat}, ξ_{typ}) , respectively. The joint bivariate distribution $n(\xi_{stat}, \xi_{typ})$ can have only six values for the different possible combinations (u, v) of the two discrete particle properties $\xi_{stat} = \xi_{stat,u}$ and $\xi_{typ} = \xi_{typ,v}$. The reader may be referred to Salenbauch (2018) for further details. This simplification can be exploited in combination with the conditional density function definition to transform Eq. 1 into a system of six bivariate NDFs $\Pi_{(u,v)}$

$$\Pi_{(u,v)}(\xi_{nc}, \xi_{H/C}) = f_{H/C}^{u,v}(\xi_{H/C}|\xi_{nc}) \cdot f_{nc}^{u,v}(\xi_{nc}) \cdot n_{u,v}, \quad (2)$$

in which the conditional distribution $f_{H/C}^{u,v}(\xi_{H/C}|\xi_{nc})$ and the marginal distribution $f_{nc}^{u,v}(\xi_{nc})$ are evaluated for each of the six combinations of (u, v) .

The set of NDFs is not solved directly but only for a set of its statistical moments closed with the CQMOM approach. In this work, for all six combinations (u, v) two quadrature nodes are used for the internal coordinate ξ_{nc} and a single quadrature node for $\xi_{H/C}$ conditioned on ξ_{nc} . The system of six bivariate NDFs is therefore represented by 36 additional moment transport

equations. The numerical calculations have been performed with the in-house universal Laminar Flame (ULF) solver (Zschutschke et al., 2017), which includes the QMOM library (Salenbauch, 2018). The conservation equations for each individual species in the gas-phase and the equations of the moments representing the solid-phase are solved using a segregated approach. Small PAH species, from benzene to pyrene, and the species involved in the surface growth, oxidation and dehydrogenation reactions (H, OH, H₂, H₂O, C₂H₂, HCO, CO, O₂) are required for the calculation of the soot moments and their gas-phase chemistry is coupled with the soot chemistry. Herein, constant species and temperature fields are applied when evaluating the soot moments, while a constant set of moments and species consumption rate due to soot processes are employed when solving for the gas-phase. Coupling of the equations is ensured by iteratively solving and updating both sets of equations until convergence is reached. Due to the stiffness of the system of equations, a pseudo-time step procedure is applied to solve the one-dimensional stationary flame to ensure numerical stability. Additionally, the spatial coordinate of the one-dimensional flame can be transformed into a residence time (Blanquart, 2008; Salenbauch, 2018) allowing to solve the set of moment equations in terms of a homogeneous zero-dimensional reactor prescribing the species fields and thermophysical properties of the gas-phase in dependence of the residence time.

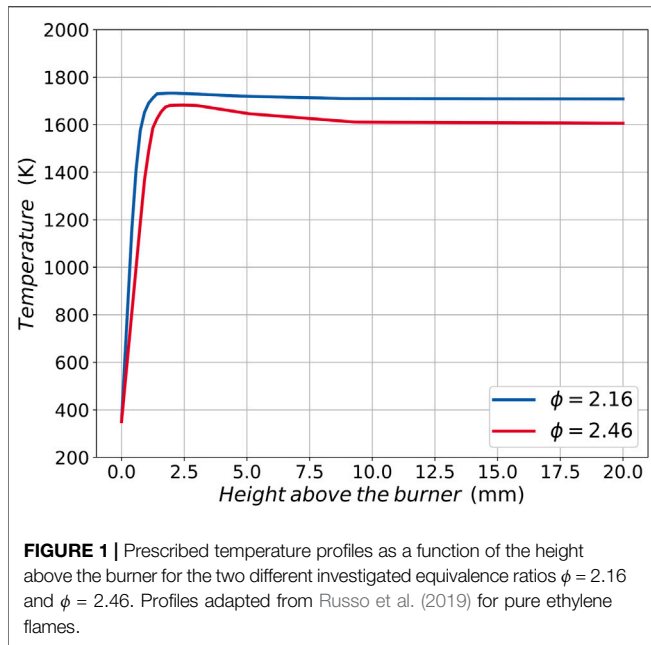
The CQMOM method does not provide access to the PSD information but it reconstructs the moments of the NDF using weighted Dirac-delta functions. Following Salenbauch et al. (2018), the entropy maximization (EM) concept is used here in post-processing to evaluate a continuous distribution of the particle sizes from a given number of moments, without prescribing the distribution shape. The idea from Mead and Papanicolaou (1984) is to find a univariate continuous distribution function $f(\xi_1)$ that maximizes the entropy (Shannon, 1948) $H(f)$, being ξ_1 the internal coordinate

$$H(f) = - \int_{\Omega_{\xi_1}} f(\xi_1) \ln(f(\xi_1)) d\xi_1. \quad (3)$$

Mead and Papanicolaou (1984) formulated the entropy for the unknown distribution function using Lagrangian multipliers and specified the moment set as constraints. This allows an explicit expression of the distribution function, which can be iteratively calculated by searching for its maximum. Further details on the numerical approach can be found in Salenbauch et al. (2017, 2018) and references therein.

3 INVESTIGATED FLAMES

In this section, the numerical setup and the investigated flames are described. A burner-stabilized flat flame is employed in this work. The flame configuration is adopted from previous experimental studies (Salamanca et al., 2012; Sirignano et al., 2014; Conturso et al., 2017; Russo et al., 2019; Ferraro et al., 2021) which used a capillary burner with an inner diameter of 5.8 cm



including a stainless steel plate located 30 mm above the burner exit for flame stabilization. The combustion parameters are kept constant in both sets of flames investigated, varying only the blending ratio of OME₃ and ethylene. Laminar, premixed conditions at atmospheric pressure and a cold gas velocity of 0.1 m/s are considered, allowing a one-dimensional simulation approach. Two equivalence ratios, $\phi = 2.16$ and $\phi = 2.46$, are investigated based on neat ethylene flames investigated in a previous study (Ferraro et al., 2021), representing lightly and highly sooting conditions. More specifically, for neat ethylene fuel, the flame at $\phi = 2.16$ presents minor formation of soot aggregates, while the flame at $\phi = 2.46$ presents a significant amount of soot aggregate and a distinct bimodality of the PSD.

Temperature profiles experimentally measured in Russo et al. (2019) for the pure ethylene flames at corresponding equivalence ratios, are prescribed for all the simulations and are plotted in **Figure 1**. As with other alternative fuels (Conturso et al., 2017), the effect that adding smaller amounts of OME₃ up to 30% exerts on the flame temperature is assumed to be insignificant, while major effects are expected when higher percentages are used. Here, this procedure is adopted to separate the thermal effects of OME₃ blending from the chemical effects in the numerical simulations.

The mixture compositions at the inlet of the flames are stated in **Table 1**. Fuel compositions are investigated ranging from pure ethylene up to pure OME₃ with intermediate blending steps. The fuel is blended by keeping the overall carbon stream constant for all flames, while the relative amount of carbon atoms provided as OME₃ compared to the overall carbon fed to the flame is specified in the table. The oxygen (O₂) stream is adapted to match the equivalence ratios of $\phi = 2.16$ and $\phi = 2.46$. The fuel and oxygen streams are diluted with nitrogen (N₂) which is adapted to ensure there is an identical cold gas velocity in all the flames. Since the combustion parameters are kept constant for all flames in this study, all the changes regarding the soot formation can be

TABLE 1 | Inflow mixture compositions of the investigated flames. Entries for 15 to 90 %_{carbon} of OME₃ blending are omitted for brevity.

ϕ	OME ₃ blending ratio	Inflow composition in mole fractions			
	in % _{carbon}	C ₂ H ₄	O ₂	N ₂	OME ₃
	0	0.131	0.182	0.686	0.000
	5	0.125	0.181	0.692	0.003
	10	0.118	0.179	0.698	0.005
2.16	5% steps
	95	0.007	0.148	0.796	0.050
	100	0.000	0.146	0.802	0.053
	0	0.147	0.179	0.674	0.000
	5	0.140	0.177	0.680	0.003
	10	0.132	0.176	0.686	0.006
2.46	5% steps
	95	0.007	0.145	0.792	0.056
	100	0.000	0.143	0.798	0.059

associated with the difference in the fuel composition and fuel structure. While a previous study Ferraro et al. (2021) compared the numerical model against experimental data, this study extends the variation of the investigated parameters and sets its focus on the blending ratio between OME₃ and C₂H₄ using the same modeling approach. In Ferraro et al. (2021), the soot reduction trends of OME₃ observed in the experiments on flames with different equivalence ratios have been well captured by the numerical method. Additionally, this burner configuration has been employed to evaluate several oxygenated fuels and their sooting characteristics (Salamanca et al., 2012; Sirignano et al., 2014; Conturso et al., 2017; Russo et al., 2019), enabling cross-comparisons to be made.

4 RESULTS AND DISCUSSION

4.1 Gas-phase

In this section, the simulation results for the gas-phase are first analyzed. **Figure 2** shows the species mole fraction profiles for C₂H₂ and C₆H₆ based on the example of two different blending ratios of pure ethylene and 50% OME₃ blending ratio with equivalence ratios of $\phi = 2.16$ in **Figure 2A** and $\phi = 2.46$ in **Figure 2B**. It is observed that 50% OME₃ blending significantly reduces the mole fraction profiles of C₂H₂ and C₆H₆ for both equivalence ratios. In the OME₃ blended flame, both species are reduced by a factor of approximately 40–50% compared to the pure ethylene flame. Additionally, the shape of the C₆H₆ profile changes in the richer flame configuration since the peak visible in the pure ethylene flame vanishes with 50% OME₃ blending.

To investigate the whole range of blending ratios, only the maximum values of the species profiles are considered in the following. In **Figure 3** the maximum value of the calculated mole fraction profiles for acetylene (C₂H₂), benzene (C₆H₆), naphthalene (C₁₀H₈) and pyrene (C₁₆H₁₀) are plotted against increasing amounts of OME₃ blended into the ethylene flame for both equivalence ratios, $\phi = 2.16$ and $\phi = 2.46$. These species have been selected because of their important role in particle inception

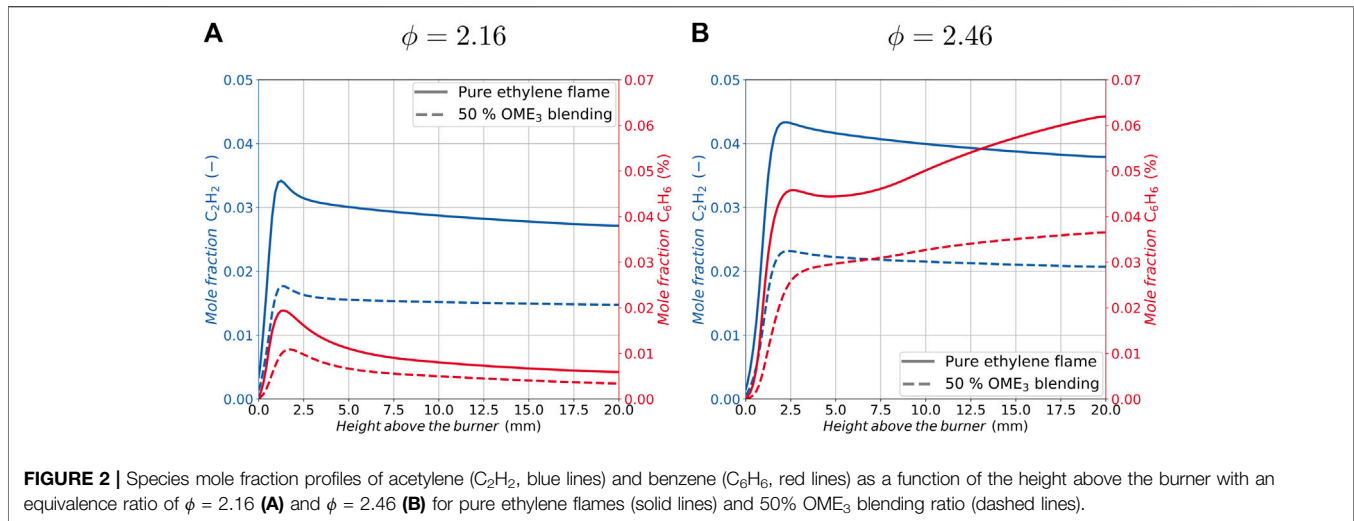


FIGURE 2 | Species mole fraction profiles of acetylene (C_2H_2 , blue lines) and benzene (C_6H_6 , red lines) as a function of the height above the burner with an equivalence ratio of $\phi = 2.16$ (A) and $\phi = 2.46$ (B) for pure ethylene flames (solid lines) and 50% OME₃ blending ratio (dashed lines).

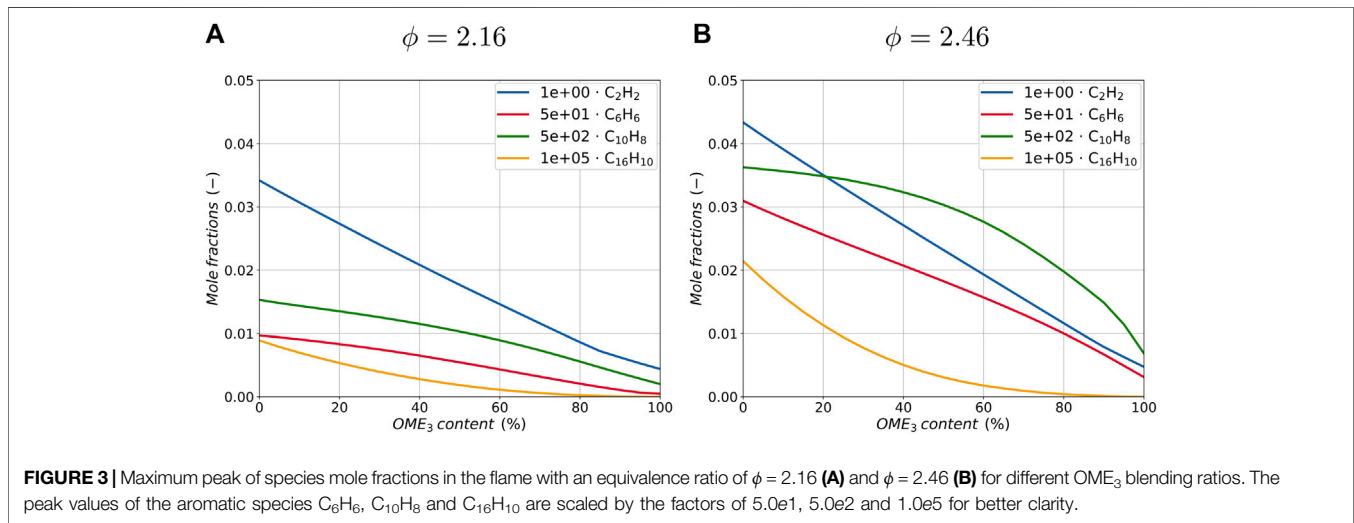


FIGURE 3 | Maximum peak of species mole fractions in the flame with an equivalence ratio of $\phi = 2.16$ (A) and $\phi = 2.46$ (B) for different OME₃ blending ratios. The peak values of the aromatic species C_6H_6 , $C_{10}H_8$ and $C_{16}H_{10}$ are scaled by the factors of $5.0e1$, $5.0e2$ and $1.0e5$ for better clarity.

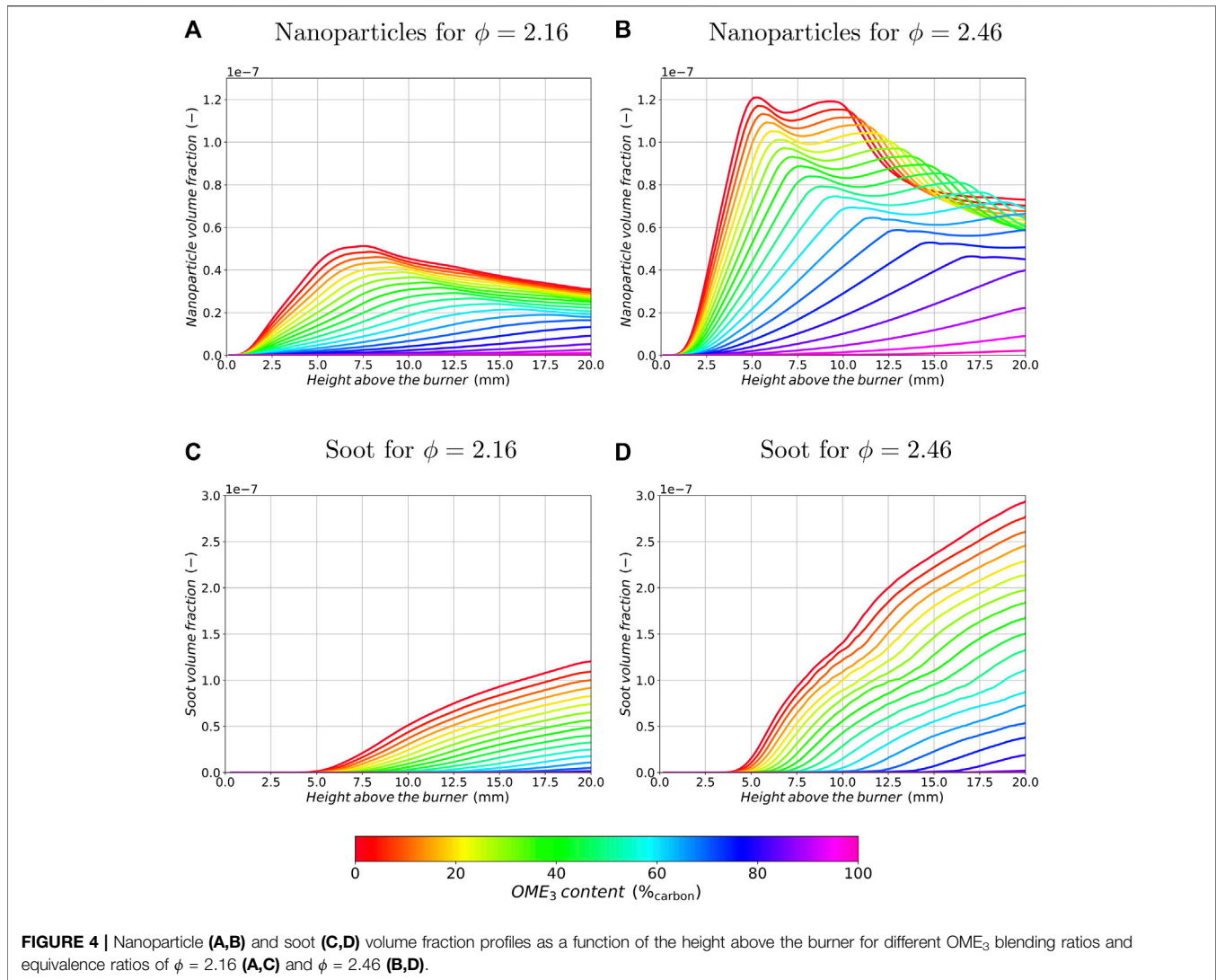
and surface growth processes. Since the evolution of larger PAHs is accounted for by the statistical soot model as described above, here only small aromatic species are plotted for both flame configurations. Acetylene can be formed from ethylene by thermal decomposition through the cleavage of two hydrogen atoms within only a few reactions, thus resulting in higher mole fractions of acetylene with increasing amounts of ethylene in the fuel. OME₃ by contrast, does not feature direct single or double carbon-to-carbon bonds in the molecule and there is no direct pathway from OME₃ forming alkenes (He et al., 2018). This results in lower mole fractions of acetylene due to OME₃ blending in both flame configurations and overall higher quantities of acetylene in the richer flame. Following C_2H_2 profiles, aromatic species are also reduced with OME₃ blending. Comparing the results for the two equivalence ratios, it can be observed that the absolute amount of C_2H_2 does not change significantly, while the flame at an equivalence ratio $\phi = 2.16$ lacks aromatic species. Therefore, it is assumed that the soot formation in the richer flame is mainly dominated by surface growth through the HACA mechanism, while the soot formation in the leaner flame is

mainly limited by the initial inception step and therefore by the amount of PAH formation.

4.2 Soot Formation

Following previous works (Salenbauch et al., 2017, 2018; Ferraro et al., 2021), the simulated PSD obtained with CQMOM and EM is split in a post-processing step to account for nanoparticles with diameters $d_p < d_{p,split}$ and aggregates with diameters $d_p > d_{p,split}$. The separation between nanoparticles and aggregates allows a more detailed analysis of the blending effect on the formation of incipient young soot particles and larger soot particles. To lower the sensitivity of this splitting diameter $d_{p,split}$, the calculations are performed for $d_{p,split} = 2$ nm and for $d_{p,split} = 7$ nm, but only the average of the two quantities is plotted in the following graphs for better clarity.

Figure 4 shows the soot volume fraction over the height above the burner for different blending ratios of OME₃ for both equivalence ratios, $\phi = 2.16$ (left) and $\phi = 2.46$ (right). The soot volume fraction of smaller nanoparticles is plotted in the two upper graphs (Figures 4A,B), while the soot volume fraction



originating from larger soot aggregates is visualized in the lower ones (Figures 4C,D). It can be observed that the nanoparticle volume fraction in Figures 4A,B increases rapidly for the pure ethylene flame until a maximum is reached at HAB = 5 mm to HAB = 7 mm depending on the equivalence ratio. Starting from HAB = 7 mm in the leaner and HAB = 10 mm in the richer flame, the particle growth becomes predominant over the inception processes resulting in a decreasing nanoparticle volume fraction further downstream in the flame. With increasing OME₃ blending in the fuel, the initial nanoparticle volume fraction decreases and the position of the peak value is shifted downstream. For HAB > 10 mm, even a small increase in the nanoparticle volume fraction can be observed for OME₃ blending in the richer condition, which is consistent with the findings in (Ferraro et al., 2021). For instance, OME₃ blending results in a slightly increased amount of nanoparticles at HAB = 12.5 mm in Figure 4B for blending ratios between 0 and 50% OME₃. Overall, the formation of nanoparticles is slowed down with OME₃ blending until no significant nanoparticle formation can be identified for pure OME₃ combustion. The amount of

nanoparticles formed in the flames follows the amount of soot precursors such as PAHs and C₂H₂ formed in the gas-phase according to the above findings.

A plateau of the nanoparticle volume fraction can be identified in the richer configuration between HAB = 5 mm and HAB = 10 mm, whereas the leaner configuration exhibits a single peak with a monotonic reduction in nanoparticle volume fraction for HAB > 7.5 mm for the pure ethylene flame. Closer investigation of the richer configuration shows that the plateau with the two peaks for smaller OME₃ blending ratios can not be explained by a single soot process alone, but is the result of coexisting soot processes. Nucleation and surface growth reactions are competing against coagulation and aggregation mechanisms in this flame region. The species profile of C₆H₆ in Figure 2B suggests that a significant amount of PAH species is present in this region of the flame, resulting in a high nucleation rate not only close to the flame sheet at approx. HAB = 2 mm but also further downstream. Figure 2A shows a single peak of C₆H₆ with a monotonic reduction until the end of the domain for the leaner flame configuration indicating that

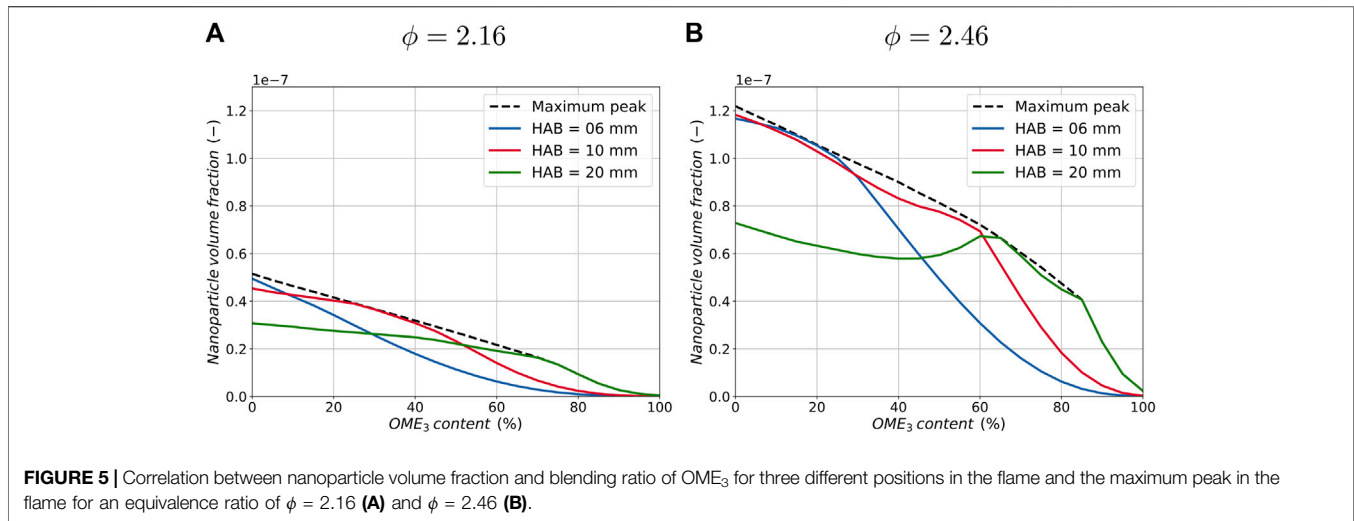


FIGURE 5 | Correlation between nanoparticle volume fraction and blending ratio of OME₃ for three different positions in the flame and the maximum peak in the flame for an equivalence ratio of $\phi = 2.16$ (A) and $\phi = 2.46$ (B).

nucleation is predominant close to the flame sheet and plays a limited role in the post-flame zone, where condensation followed by coagulation and aggregation contribute to the soot evolution.

Furthermore, in **Figures 4C,D** it can be seen that the position where aggregates start to form is shifted downstream with increasing OME₃ blending ratios and the volume fraction of large particles is significantly decreased at both equivalence ratios. Therefore, OME₃ blending results in a monotonically decreasing amount of aggregates. The slowing down of the particle formation processes follows the decrease and delay of nanoparticle formation and is also similar to other biofuels such as ethanol or dimethyl ether (Salamanca et al., 2012; Sirignano et al., 2014).

Figure 5 shows the correlation between the nanoparticle volume fraction and the OME₃ content in the fuel for three different positions in the flame for both equivalence ratios. Additionally, the maximum value of the nanoparticle volume fraction of the whole flame is added in the graphs, which allows the results to be analyzed regardless of the position in the flame.

At a position of HAB = 6 mm and HAB = 10 mm, the nanoparticle volume fraction evolves similarly for both equivalence ratio flames. It is monotonically reduced with increasing OME₃ blending ratios. In contrast, at a position of HAB = 20 mm, a non-monotonic evolution of the nanoparticle reduction with increasing blending ratios can be observed in the richer flame configuration, while the leaner flame configuration exhibits no substantial change unless high blending ratios close to neat OME₃ are burnt. Here, no substantial change in nanoparticle volume fraction can be identified for OME₃ contents between 0% and approximately 70% for both equivalence ratios. Further increasing the OME₃ content reduces the nanoparticle volume fraction again. Comparing the three curves of the different positions in the flames for both equivalence ratios, they are all seen to share a flat gradient for smaller blending ratios and a steep decline in nanoparticle volume fraction for increasing blending ratios at increased HABs. These results indicate that even if the nanoparticles decrease locally, the number of nanoparticles downstream along the flame does not decrease substantially, so the particle formation is slowed down. Additionally, the

maximum peak of nanoparticles in the flame indicates that a significant reduction in the amount of nanoparticles, equivalent to a larger gradient of the maximum peak, can only be obtained for larger blending ratios. A monotonic reduction in the maximum peak can be observed in both flames, with a rapid drop for blending ratios larger than approximately 70% OME₃ blending. This effect is true for both configurations, whereas the overall reduction in nanoparticles due to OME₃ blending is larger in the richer configuration. Meanwhile, only a small reduction can be observed in the lean configuration for the same OME₃ percentages.

Figure 6 shows the soot volume fraction originating from large aggregates over the OME₃ blending ratio of three locations along both flame configurations. At all three positions in the flame, OME₃ blending reduces the formation of aggregates until a complete suppression is observed for a specific flame position in both flame configurations. The quantitative correlation between the amount of OME₃ in the fuel and soot volume fraction is approximately linear in the case of the rich flame configuration in **Figure 6B**. Additionally, the gradient of the three curves changes for the different positions in the flame, resulting in a larger soot reduction further downstream in the flame when the same amount of OME₃ is added. For soot (large particles and aggregates), there is a direct correlation with the C₂H₂ concentration, since surface growth plays a dominant role at the investigated equivalence ratio of $\phi = 2.46$.

At the lower equivalence ratio, **Figure 6A**, a decreasing aggregate reduction effect can be observed with increasing amounts of OME₃ blending. This results in slightly regressively declining soot volume fraction slopes compared to the almost linear behavior of the rich conditions. This is thought to be due to the leaner conditions, in which nucleation is one of the limiting factors in the soot formation process. Therefore, the shape of the curves follows the shape of larger PAHs such as pyrene and is less heavily influenced by surface growth reactions of C₂H₂. Overall, both configurations show a significant reduction in soot aggregates for OME₃ blending with a monotonic effect for all ratios throughout the flame.

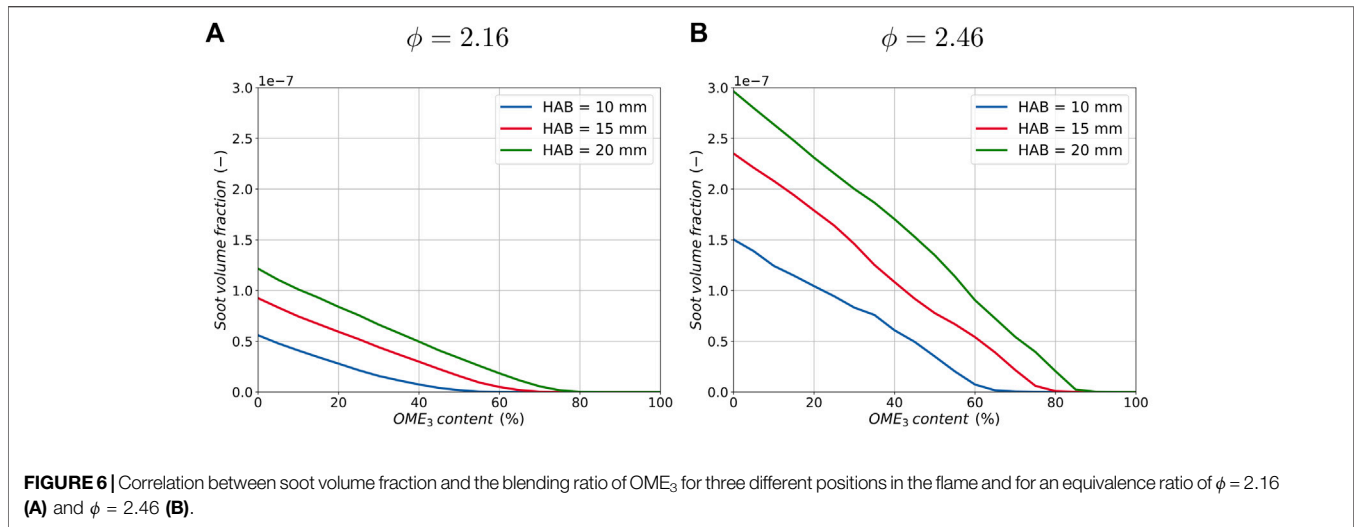


FIGURE 6 | Correlation between soot volume fraction and the blending ratio of OME₃ for three different positions in the flame and for an equivalence ratio of $\phi = 2.16$ (A) and $\phi = 2.46$ (B).

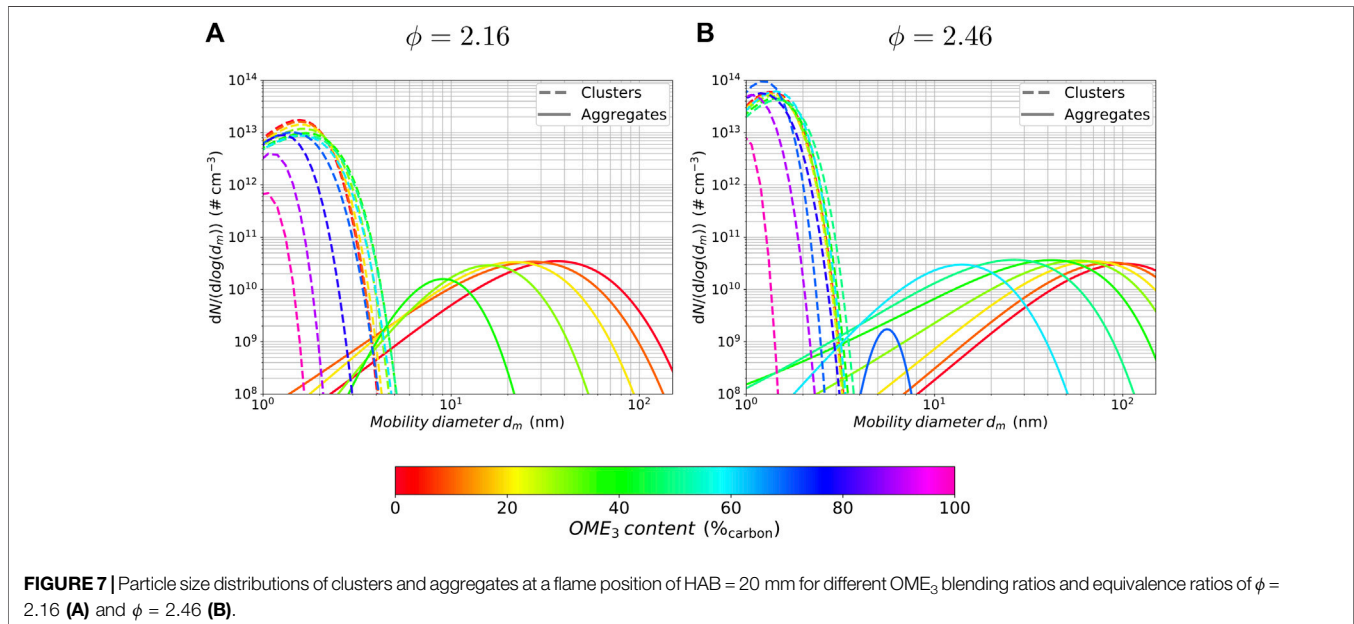


FIGURE 7 | Particle size distributions of clusters and aggregates at a flame position of HAB = 20 mm for different OME₃ blending ratios and equivalence ratios of $\phi = 2.16$ (A) and $\phi = 2.46$ (B).

To evaluate the effect of different OME₃ blending ratios on the particle sizes and their distribution, **Figure 7** shows the particle size distribution (PSD) that is obtained by the entropy maximization process at HAB = 20 mm. Blending steps with 10%_{carbon} are used and larger PAHs are omitted to enhance readability. A distinction is made between spherical clusters and fractal-shaped aggregates, which are plotted over the mobility diameter d_m . The mobility diameter d_m considers the fractal-like shape of larger soot aggregates in contrast to the spherical diameter d_p , which assumes a purely spherical particle. The mobility diameter is derived from the collision diameter d_c with $d_m \equiv d_c = d_p(n_p)^{1/D_f}$ (Kruis et al., 1993). A fractal dimension D_f equal to 1.8 and a primary particle diameter of $d_p = 15$ nm are applied and the number of primary particles n_p is derived from the mass ratio of an aggregate and the corresponding primary particles. This procedure, previously used in (Ferraro et al., 2021), is applied here

to allow for a consistent comparison with our previous studies. Note that the selected parameters are comparable with the common values used in the literature (Kruis et al., 1993).

It can be seen that the distribution of the particle clusters is not substantially changed for an OME₃ blending ratio between 0 and 60% in both flame configurations. Further increasing the OME₃ content for the rich condition results in a higher number of particles with smaller diameters, and further on, in a significant decrease in the number and size of the clusters for conditions close to neat OME₃ combustion, while no such large intermediate increase in the number of clusters is visible in the leaner flame configuration of $\phi = 2.16$ in **Figure 7A**. This difference is consistent with the findings of the nanoparticle volume fraction in **Figures 4A,B** at a height of HAB = 15 mm, in which the leaner flame configuration shows a monotonic decrease of nanoparticle volume fraction with increasing OME₃ blending, whereas the

richer configuration exhibits a non-monotonic behaviour with an intermediate increase in nanoparticle volume fraction. Similar non-monotonic behavior was found previously for premixed propene flames blended with ethylene (Lin et al., 2018), in which small amounts of ethylene addition led to an intermediate increase in soot formation while larger amounts decreased the amount of soot. It was found that this effect is due to a synergistic effect of the two fuels by the acetylene addition and propargyl recombination/addition pathways (Lin et al., 2018).

The distribution of aggregates in the richer configuration in **Figure 7B** indicates that there are significant changes regarding the overall number and particle diameter with an increasing OME₃ content. A considerable amount of aggregate formation occurs for OME₃ blending ratios of $\leq 70\%$, while higher contents of OME₃ in the fuel delay the soot formation and suppress aggregate formation to a negligible level. The distribution function therefore changes from a bimodal to a unimodal shape. While the number of aggregates differs only slightly in the range of 60–0% OME₃, with a maximum at approximately 50% OME₃, the size of the particles changes significantly from an average mobility diameter of approx. 15 nm to 100 nm. For blending percentages above 60%, the number of aggregates is additionally reduced. In contrast to that, the aggregates show a simultaneous reduction in number and diameter even for small blending ratios of OME₃ in the leaner flame configuration, with a suppression to negligible levels for blending ratios of above 40% OME₃.

Further investigations at upstream positions in the flame show that the PSD changes its shape, from bimodal to unimodal, for lower levels of the OME₃ blending ratio.

5 CONCLUSION

A numerical study is performed simulating two series of laminar premixed burner-stabilized flames burning a mixture of C₂H₄ and OME₃ for two equivalence ratios, corresponding to highly and lightly sooting flame conditions. The sets cover flames with increasing blending ratios of OME₃ reaching from pure ethylene to pure OME₃ at a constant equivalence ratio and identical carbon streams. The soot precursors in the gas-phase, soot formation and PSD are analyzed using a detailed physico-chemical soot model.

The effects of OME₃ blending are found to be different for nanoparticles compared to larger aggregates. While the formation of larger aggregates is approximately linearly reduced for

increasing amounts of OME₃ throughout the flame, the nanoparticle formation shows a non-monotonic correlation to the blending ratio and is mainly suppressed for higher amounts of OME₃, similarly to the combustion of pure OME₃.

The particle size distribution is reconstructed with the concept of entropy maximization at a fixed height above the burner of HAB = 20 mm. A substantially unchanged distribution of clusters for OME₃ blending ratios between approximately 0 and 60% and a decreasing number of particles for higher blending percentages can be identified for both equivalence ratios with a slight, intermediate increase in the particle number for the richer flame condition at around 70% OME₃ in the fuel, whereas the leaner configuration shows a monotonic reduction in the particle number. While the number of aggregates in the richer configuration is not significantly affected by smaller amounts of OME₃ blending, their particle size is mainly reduced, but a simultaneous reduction in the particle number and particle diameter is observed for the leaner configuration at this position in the flame.

These findings indicate that OME₃ blending mainly delays the soot formation processes and, as a consequence, suppresses the formation of larger aggregates at a specific position in the flame. This is due to the absence of direct carbon-to-carbon bonds in OME₃, which leads to a more complete oxidation process and therefore subtracts carbon from the soot growth pathways. The linear correlation for aggregate reduction suggests a predominant dilution effect rather than an active kinetic effect.

DATA AVAILABILITY STATEMENT

The raw data supporting the conclusion of this article will be made available by the authors, without undue reservation.

AUTHOR CONTRIBUTIONS

RS, MS and FF contributed to conceptualization, writing - review and editing. CH contributed to conceptualization, review - editing and funding acquisition.

FUNDING

The authors gratefully acknowledge the funding by the German Federal Ministry of Education and Research (BMBF) as part of the NAMOSYN Project (project number 03SF0566R0).

REFERENCES

- Bai, J., Geeson, R., Farazi, F., Mosbach, S., Akroyd, J., Bringley, E. J., et al. (2021). Automated Calibration of a Poly(oxyethylene) Dimethyl Ether Oxidation Mechanism Using the Knowledge Graph Technology. *J. Chem. Inf. Model.* 4, 1701–1717. doi:10.1021/acs.jcim.0c01322
- Barro, C., Parravicini, M., Boulouchos, K., and Liati, A. (2018). Neat polyoxyethylene dimethyl ether in a diesel engine; part 2: Exhaust emission analysis. *Fuel* 234, 1414–1421. doi:10.1016/j.fuel.2018.07.108
- Blanquart, G. G. (2008). *Chemical and Statistical Soot modeling*. California: Ph.D. thesis, Stanford University.
- Bokinge, P., Heyne, S., and Harvey, S. (2020). Renewable OME from biomass and electricity-Evaluating carbon footprint and energy performance. *Energy Sci. Eng.* 8, 2587–2598. doi:10.1002/ese3.687
- Cai, L., Jacobs, S., Langer, R., vom Lehn, F., Heufer, K. A., and Pitsch, H. (2020). Auto-ignition of oxymethylene ethers (OMEn, n = 2-4) as promising synthetic e-fuels from renewable electricity: shock tube experiments and automatic mechanism generation. *Fuel* 264, 116711. doi:10.1016/j.fuel.2019.116711

- Conturso, M., Sirignano, M., and D'Anna, A. (2017). Effect of 2,5-dimethylfuran doping on particle size distributions measured in premixed ethylene/air flames. *Proc. Combustion Inst.* 36, 985–992. doi:10.1016/j.proci.2016.06.048
- D'Anna, A., Sirignano, M., and Kent, J. (2010). A model of particle nucleation in premixed ethylene flames. *Combust. Flame* 157, 2106–2115. doi:10.1016/j.combustflame.2010.04.019
- Deutsch, D., Oestreich, D., Lautenschütz, L., Haltenort, P., Arnold, U., and Sauer, J. (2017). High Purity Oligomeric Oxymethylene Ethers as Diesel Fuels. *Chem. Ingenieur Technik* 89, 486–489. doi:10.1002/cite.201600158
- Ferraro, F., Russo, C., Schmitz, R., Hasse, C., and Sirignano, M. (2021). Experimental and numerical study on the effect of oxymethylene ether-3 (OME3) on soot particle formation. *Fuel* 286, 119353. doi:10.1016/j.fuel.2020.119353
- Gierlich, C. H., Beydoun, K., Klankermayer, J., and Palkovits, R. (2020). Challenges and Opportunities in the Production of Oxymethylene Dimethylether. *Chem. Ingenieur Technik* 92, 116–124. doi:10.1002/cite.201900187
- He, T., Wang, Z., You, X., Liu, H., Wang, Y., Li, X., et al. (2018). A chemical kinetic mechanism for the low- and intermediate-temperature combustion of Polyoxymethylene Dimethyl Ether 3 (PODE3). *Fuel* 212, 223–235. doi:10.1016/j.fuel.2017.09.080
- Huang, H., Liu, Q., Teng, W., Pan, M., Liu, C., and Wang, Q. (2018). Improvement of combustion performance and emissions in diesel engines by fueling n-butanol/diesel/PODE3-4 mixtures. *Appl. Energy* 227, 38–48. doi:10.1016/j.apenergy.2017.09.088
- Klokic, S., Hochegger, M., Schober, S., and Mittelbach, M. (2020). Investigations on an efficient and environmentally benign poly(oxymethylene) dimethyl ether (OME3-5) fuel synthesis. *Renew. Energy* 147, 2151–2159. doi:10.1016/j.renene.2019.10.004
- Kohse-Höinghaus, K. (2021). Combustion in the future: The importance of chemistry. *Proc. Combustion Inst.* 38, 1–56. doi:10.1016/j.proci.2020.06.375
- Kruis, F. E., Kusters, K. A., Pratsinis, S. E., and Scarlett, B. (1993). A Simple Model for the Evolution of the Characteristics of Aggregate Particles Undergoing Coagulation and Sintering. *Aerosol Sci. Tech.* 19, 514–526. doi:10.1080/02786829308959656
- Lautenschütz, L., Oestreich, D., Seidenspinner, P., Arnold, U., Dinjus, E., and Sauer, J. (2016). Physico-chemical properties and fuel characteristics of oxymethylene dialkyl ethers. *Fuel* 173, 129–137. doi:10.1016/j.fuel.2016.01.060
- LeBlanc, S., Sandhu, N., Yu, X., Han, X., Wang, M., Tjong, J., et al. (2020). “An Investigation Into OME3 on a High Compression Ratio Engine,” in ASME 2020 Internal Combustion Engine Division Fall Technical Conference. Internal Combustion Engine Division Fall Technical Conference. doi:10.1115/ICEF2020-2983 Available at: <https://asmedigitalcollection.asme.org/ICEF/proceedings-pdf/ICEF2020/84034/V001T02A007/6603497/v001t02a007-icef2020-2983.pdf>
- Li, R., Herreros, J. M., Tsolakis, A., and Yang, W. (2020). Chemical kinetic study on ignition and flame characteristic of polyoxymethylene dimethyl ether 3 (PODE3). *Fuel* 279, 118423. doi:10.1016/j.fuel.2020.118423
- Lin, B., Gu, H., Ni, H., Guan, B., Li, Z., Han, D., et al. (2018). Effect of mixing methane, ethane, propane and ethylene on the soot particle size distribution in a premixed propene flame. *Combustion and Flame* 193, 54–60. doi:10.1016/j.combustflame.2018.03.002
- Lin, Q., Tay, K. L., Zhou, D., and Yang, W. (2019). Development of a compact and robust Polyoxymethylene Dimethyl Ether 3 reaction mechanism for internal combustion engines. *Energy Convers. Manag.* 185, 35–43. doi:10.1016/j.enconman.2019.02.007
- Liu, H., Wang, Z., Li, Y., Zheng, Y., He, T., and Wang, J. (2019). Recent progress in the application in compression ignition engines and the synthesis technologies of polyoxymethylene dimethyl ethers. *Appl. Energy* 233–234, 599–611. doi:10.1016/j.apenergy.2018.10.064
- Lumpp, B., Rothe, D., Pastötter, C., Lämmermann, R., and Jacob, E. (2011). Oxymethylene Ethers as Diesel Fuel Additives of the Future. *MTZ Worldw* 72, 34–38. doi:10.1365/s38313-011-0027-z
- Lv, D., Chen, Y., Chen, Y., Guo, X., Chen, H., and Huang, H. (2019). Development of a reduced diesel/PODEn mechanism for diesel engine application. *Energy Convers. Manag.* 199, 112070. doi:10.1016/j.enconman.2019.112070
- Mahbub, N., Oyedun, A. O., Zhang, H., Kumar, A., and Pogonietz, W.-R. (2019). A life cycle sustainability assessment (LCSA) of oxymethylene ether as a diesel additive produced from forest biomass. *Int. J. Life Cycle Assess.* 24, 881–899. doi:10.1007/s11367-018-1529-6
- Mead, L. R., and Papanicolaou, N. (1984). Maximum entropy in the problem of moments. *J. Math. Phys.* 25, 2404–2417. doi:10.1063/1.526446
- Niu, B., Jia, M., Chang, Y., Duan, H., Dong, X., and Wang, P. (2021). Construction of reduced oxidation mechanisms of polyoxymethylene dimethyl ethers (PODE1-6) with consistent structure using decoupling methodology and reaction rate rule. *Combustion and Flame* 232, 111534. doi:10.1016/j.combustflame.2021.111534
- Omari, A., Heuser, B., Pischinger, S., and Rüdinger, C. (2019). Potential of long-chain oxymethylene ether and oxymethylene ether-diesel blends for ultra-low emission engines. *Appl. Energy* 239, 1242–1249. doi:10.1016/j.apenergy.2019.02.035
- Parravicini, D., Barro, C., and Boulouchos, K. (2020). Compensation for the differences in LHV of diesel-OME blends by using injector nozzles with different number of holes: Emissions and combustion. *Fuel* 259, 116166. doi:10.1016/j.fuel.2019.116166
- Pélerin, D., Gaukel, K., Härtl, M., Jacob, E., and Wachtmeister, G. (2020). Potentials to simplify the engine system using the alternative diesel fuels oxymethylene ether OME1 and OME3–6 on a heavy-duty engine. *Fuel* 259, 116231. doi:10.1016/j.fuel.2019.116231
- Pellegrini, L., Marchionna, M., Patrini, R., and Florio, S. (2013). “Emission performance of neat and blended polyoxymethylene dimethyl ethers in an old light-duty diesel car,” in SAE 2013 World Congress & Exhibition SAE International 2, 1–12. doi:10.4271/2013-01-1035
- Ren, S., Wang, Z., Li, B., Liu, H., and Wang, J. (2019). Development of a reduced polyoxymethylene dimethyl ethers (PODEn) mechanism for engine applications. *Fuel* 238, 208–224. doi:10.1016/j.fuel.2018.10.111
- Russo, C., D'Anna, A., Ciajolo, A., and Sirignano, M. (2019). The effect of butanol isomers on the formation of carbon particulate matter in fuel-rich premixed ethylene flames. *Combustion and Flame* 199, 122–130. doi:10.1016/j.combustflame.2018.10.025
- Salamanca, M., Sirignano, M., Commodo, M., Minutolo, P., and D'Anna, A. (2012). The effect of ethanol on the particle size distributions in ethylene premixed flames. *Exp. Therm. Fluid Sci.* 43, 71–75. doi:10.1016/j.expthermflusci.2012.04.006
- Salenbauch, S. (2018). *Modeling of Soot Formation and Oxidation in Reacting Flows*. TU Darmstadt: Ph.D. thesis.
- Salenbauch, S., Sirignano, M., Marchisio, D. L., Pollack, M., D'Anna, A., and Hasse, C. (2017). Detailed particle nucleation modeling in a sooting ethylene flame using a Conditional Quadrature Method of Moments (CQMOM). *Proc. Combustion Inst.* 36, 771–779. doi:10.1016/j.proci.2016.08.003
- Salenbauch, S., Sirignano, M., Pollack, M., D'Anna, A., and Hasse, C. (2018). Detailed modeling of soot particle formation and comparison to optical diagnostics and size distribution measurements in premixed flames using a method of moments. *Fuel* 222, 287–293. doi:10.1016/j.fuel.2018.02.148
- Shannon, C. E. (1948). A Mathematical Theory of Communication. *Bell Syst. Tech. J.* 27, 379–423. doi:10.1002/j.1538-7305.1948.tb01338.x
- Sirignano, M., Kent, J., and D'Anna, A. (2010). Detailed modeling of size distribution functions and hydrogen content in combustion-formed particles. *Combustion and Flame* 157, 1211–1219. doi:10.1016/j.combustflame.2009.11.014
- Sirignano, M., Kent, J., and D'Anna, A. (2013). Modeling formation and oxidation of soot in nonpremixed flames. *Energy Fuels* 27, 2303–2315. doi:10.1021/ef400057r
- Sirignano, M., Salamanca, M., and D'Anna, A. (2014). The role of dimethyl ether as substituent to ethylene on particulate formation in premixed and counter-flow diffusion flames. *Fuel* 126, 256–262. doi:10.1016/j.fuel.2014.02.039
- Sun, W., Wang, G., Li, S., Zhang, R., Yang, B., Yang, J., et al. (2017). Speciation and the laminar burning velocities of poly(oxymethylene) dimethyl ether 3 (POMDME3) flames: An experimental and modeling study. *Proc. Combustion Inst.* 36, 1269–1278. doi:10.1016/j.proci.2016.05.058
- Tan, Y. R., Salamanca, M., Pascazio, L., Akroyd, J., and Kraft, M. (2021). The effect of poly(oxymethylene) dimethyl ethers (PODE3) on soot formation in ethylene/PODE3 laminar coflow diffusion flames. *Fuel* 283, 118769. doi:10.1016/j.fuel.2020.118769
- Wang, Z., Liu, H., Ma, X., Wang, J., Shuai, S., and Reitz, R. D. (2016). Homogeneous charge compression ignition (HCCI) combustion of

polyoxymethylene dimethyl ethers (PODE). *Fuel* 183, 206–213. doi:10.1016/j.fuel.2016.06.033

Zheng, Y., Tang, Q., Wang, T., Liao, Y., and Wang, J. (2013). Synthesis of a green fuel additive over cation resins. *Chem. Eng. Technol.* 36, 1951–1956. doi:10.1002/ceat.201300360

Zschutschke, A., Messig, D., Scholtissek, A., and Hasse, C. (2017). *Universal Laminar Flame Solver (ULF)* Freiberg. Available at: https://figshare.com/articles/ULF_code_pdf/5119855.

Conflict of Interest: The authors declare that the research was conducted in the absence of any commercial or financial relationships that could be construed as a potential conflict of interest.

Publisher's Note: All claims expressed in this article are solely those of the authors and do not necessarily represent those of their affiliated organizations, or those of the publisher, the editors and the reviewers. Any product that may be evaluated in this article, or claim that may be made by its manufacturer, is not guaranteed or endorsed by the publisher.

Copyright © 2021 Schmitz, Sirignano, Hasse and Ferraro. This is an open-access article distributed under the terms of the Creative Commons Attribution License (CC BY). The use, distribution or reproduction in other forums is permitted, provided the original author(s) and the copyright owner(s) are credited and that the original publication in this journal is cited, in accordance with accepted academic practice. No use, distribution or reproduction is permitted which does not comply with these terms.